

Covalent Organic Frameworks

Asymmetric Diamine Synthesis for Covalent Organic Frameworks: Boosted Photocatalytic Performance by Restricting β -Ketoenamine Bond Twist

Lichao Wang⁺, Dongge Ma⁺, Aoxiang Liu, Hao Du,^{*} Yangjie Fu,^{*} Abdullah M. Al-Enizi, Ayman Nafady, Shengqian Ma,^{*} and Qi. Wang^{*}

Abstract: Covalent organic frameworks (COFs) are typically formed by the covalent bonding of geometrically symmetrical linkers. In this work, an asymmetric (C_{1h} symmetry) amine linker (2,6-diaminobenzothiazole) was employed to non-linearly connect and synthesize the COFs (TpBa) featuring β -ketoenamine bond, which lead to the discovery of interesting “angle-induced restricted twist (AIRT)” effect. Compared with the COFs TpPa and TpDa with geometrically symmetrical linkers, the presence of asymmetric amine moieties in TpBa introduced certain angles between building blocks, mitigating the twist of the molecular plane caused by spatial steric hindrance on both sides of the β -ketoenamine bonds thereby preserving the planar π -conjugated system. Although TpDa exhibited a more favorable charges structure and distribution for separation and transport, TpBa demonstrated superior H_2O_2 yield, suggesting the potential dominance of the AIRT effect under specific conditions. This work not only expands the option for COFs linker selection but also provides insights into boosting the photocatalytic performance of COFs.

Introduction

Covalent organic frameworks (COFs) are a class of organic porous crystalline materials with excellent physical and chemical stability, large specific surface area.^[1,2] These properties make them widely applicable in various fields, such as environmental remediation,^[3] catalysis^[4] and sensing.^[5] In recent years, COFs have garnered widespread attention in the field of photocatalysis due to well-defined planar π -conjugated systems, abundant donor–acceptor (D–A) units, and appropriate band structures.^[6]

The planar or spatial structures of COFs are determined by their building blocks and linkers.^[7,8] These components are predominantly composed of aromatic heterocycles that incorporate simple elements such as C, N, O, and S, which are known to induce heteroatom effects (HAE).^[9] Therefore, by substituting building blocks and linkers with specific functional groups, it is possible to regulate the active sites of the catalyst, improve energy band structure, and introduce unique characteristics and functions.^[10] Since Yaghi et al. first synthesized COFs in 2005,^[11] the number of ligands used for synthesizing COFs has been huge. Based on the theory of network chemistry and topology, most COFs ligands need to follow strict geometric symmetry. Typically, the node building blocks and linkers generally present $C_{(2,3,4,6)}$, $D_{(2,3,4,6)}$, and other symmetries,^[12,13] which can be connected in a consistent orientation to achieve long-range ordered network structure.^[14] Regardless of the linkers and symmetry combination employed, strategies such as narrowing the bandgap, optimizing the π -conjugated system, and modulating charge distribution are fundamental to boost the separation, transport, and overall photocatalytic performance of charges within COFs.^[15,16]


Due to the stability of Schiff base condensation reaction, it is one of the most widely used methods for synthesizing COFs.^[17] In most studies, the C=N bond and β -ketoenamine bond are considered to impede photocatalytic performance. In highly linearly connected COFs, steric hindrance causes planar molecules on the linkers to twist easily, disrupting the charge separation and transport within the framework.^[18,19] Therefore, converting or reinforcing bonds and utilizing intramolecular hydrogen bonding are common methods for maintaining a planar π -conjugated system. For example, Yang et al. ^[20] transformed a weak single-sided linker into a

[*] L. Wang⁺, A. Liu, Dr. H. Du, Y. Fu, Prof. Dr. Q. Wang
Zhejiang Key Laboratory of Solid Waste Pollution Control and Resource Utilization, School of Environmental Science and Engineering, Zhejiang Gongshang University, Hangzhou 310018, China
E-mail: duhao@zjgsu.edu.cn
fuyangjie@iccas.ac.cn
wangqi8327@zjgsu.edu.cn

Prof. Dr. S. Ma
Department of Chemistry, University of North Texas, Denton TX76203, USA
E-mail: Shengqian.Ma@unt.edu

Assoc. Prof. Dr. D. Ma⁺
School of Light Industry Science and Engineering, Beijing Technology and Business University, Beijing 100048, China
Assoc. Prof. Dr. A. M. Al-Enizi, Assoc. Prof. Dr. A. Nafady
Department of Chemistry, College of Science, King Saud University, Riyadh 11451, Saudi Arabia

[†] Both authors contributed equally to this work.

 Additional supporting information can be found online in the Supporting Information section

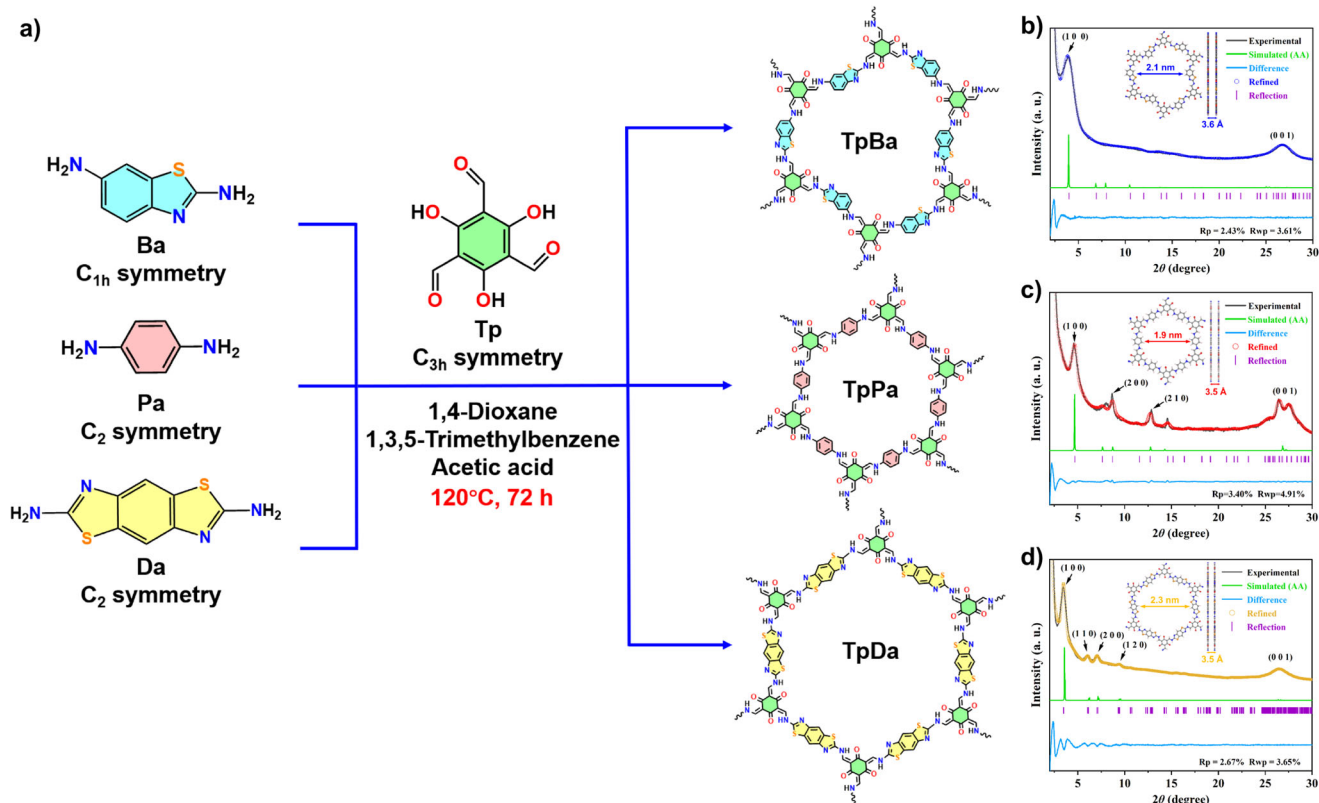


Figure 1. a) Schematic diagram of the preparation process for TpBa, TpPa and TpDa. Experimental and Pawley-refined PXRD patterns for TpBa b), TpPa c), and TpDa d). (C atoms: gray; N atoms: blue; O atoms: red; S atoms: yellow; H atoms: pink).

rigid planar linker by reacting the acryloxy group on the side chain with the C=N bond to generate a quinoline ring, thereby enhancing the π -conjugated system of the framework. Wang et al. synthesized a COF with an external –F on the linker that not only maintains a planar rigid structure through hydrogen bonding, but also promotes interlayer π - π stacking and facilitates axial charge transport.^[21] The C=N bond can undergo further reaction with the presence of a hydroxyl group to form a β -ketoenamine bond,^[22] which can generate partial intramolecular hydrogen bonding with the carbonyl group.^[23,24] However, it remains challenging to restrain molecular plane twisting on the linker. The regular linear connectivity, in conjunction with the intrinsic bonding element characteristics, imparts enhanced flexibility to the molecules within the linker. Therefore, without altering covalent bonds, utilizing asymmetric linkers to modify linear connections may serve as a method for restricting twisting.^[25]

The incorporation of new functional groups into COFs and the maintenance of planar π -conjugated systems are both intriguing research directions.^[26,27] Herein, we proposed a new strategy to synthesize a novel single pore COF TpBa connected by β -ketoenamine bond via reacting 2,6-benzothiazole diamine (Ba) with 1,3,5-triformylphloroglucinol (Tp). The amine linker in TpBa exhibited nonlinearity and C_{1h} symmetry, allowing for non-linear connections that restrict planar twisting by altering the special angles and interlayer forces between junction blocks. The C_{1h} linker undergoes a morphological adjust-

ment to facilitate its reconfiguration into a regular network structure, which ensures normal electron transport within the framework.^[28] As a control, linear-linked TpPa and TpDa were synthesized using the same method. We studied the visible-light photocatalytic performances of TpBa, TpPa, and TpDa using H_2O_2 production, the results of which highlighted the superiority of TpBa over the other two COFs. Through the combination of theoretical calculations and experimental results, the electronic structure and molecular dynamic characteristics were investigated. Our findings indicated that while the charge distribution characteristics of TpBa are not optimal, its superior photocatalytic performance revealed the significant role played by asymmetric linkers in restricting planar twisting.^[29] Building upon these observations, the contributions to maintaining planar π -conjugated systems and promoting charge movement were categorized as angle-induced restricted twist (AIRT) effect. Thus, our research will provide valuable insights into ligand selection for COFs based on C_{1h} symmetry and offered a deeper understanding of mechanisms for boosting photocatalytic processes.

Results and Discussion

Tp undergoes Schiff base condensation reactions with Ba, p-phenylenediamine (Pa) and 2,6-diaminobenzobisthiazole (Da) via solvothermal methods to yield TpBa, TpPa and TpDa, respectively. Figure 1a showed a schematic illustration

of the synthesis (for all characterizations, experimental procedures, and computational details, please refer to the Supporting Information). Powder X-ray diffraction (PXRD) and Pawley refinement analyses (Figure 1b–d) were employed to investigate the crystal structure and crystallinity. All three COFs are microcrystalline materials and display hexagonal crystal faces. TpBa showed diffraction peaks at 3.92° and 26.74° , which correspond to (1 0 0) and π - π stacking (0 0 1) crystallographic planes, respectively. The series of diffraction peaks observed at 4.66° , 8.66° , 12.46° , and 26.80° in TpPa can be attributed to the (1 0 0), (2 0 0), (2 1 0), and (0 0 1) crystallographic planes, respectively.^[30] The (1 0 0), (1 1 0), (2 0 0), (1 2 0), and (0 0 1) crystal planes of TpDa were observed at $2\theta = 3.48^\circ$, 6.06° , 7.08° , 9.36° , and 26.48° .^[31] To further analyze the crystal information, we constructed models of the three COFs and performed Pawley refinement, which showed good agreement between the observed and simulated patterns. The atomic coordinates were shown in Tables S1–S3. After comparing the experimental PXRD data with simulated PXRD data of AA and AB stacking modes (Figure S1), we found that all three COFs are closer to the AA stacking mode.

The surface morphology of TpBa, TpPa and TpDa were observed by scanning electron microscopy (SEM), and the results were shown in Figure 2a–c. All three COFs exhibited the characteristic strip-like morphology of β -ketoenamine bond COFs.^[32] Energy-dispersive X-ray spectroscopy (EDS) elemental mapping (Figure S2) revealed homogeneous distribution of all constituent elements in the three COFs. The specific surface areas and pore volumes of the three COFs were analyzed and evaluated using the N_2 sorption method at 77 K. As shown in Figure S3, all three COFs exhibited Type I adsorption-desorption isotherms, indicating a microporous structure. The Brunauer-Emmett-Teller (BET) specific surface areas of TpBa, TpPa, and TpDa were 1230.8, 635.6, and 1364.5 $m^2 g^{-1}$, respectively, with the pore size mainly distributed at 0.54, 0.50, and 0.61 nm. Besides, the total pore volumes of TpBa, TpPa and TpDa were 1.02, 0.39, and 1.54 $cm^3 g^{-1}$, respectively.

The Fourier transform infrared spectroscopy (FT-IR) spectra of TpBa, TpPa, and TpDa were analyzed and the results were shown in Figure S4. The C=O stretching vibration appeared at $1614 cm^{-1}$. The band at $1256 cm^{-1}$ indicated the C–N bending vibration.^[33] The X-ray photoelectron spectroscopy (XPS) spectra of the three COFs also used for structural characterization. In the C 1 s XPS spectrum (Figure S5a), binding energy peaks were observed at 284.8 eV (corresponding to C–C/C=C), 286.8 eV (corresponding to C–N/C–O), and 288.4 eV (corresponding to C=O). In the parts of TpBa and TpDa, the characteristic peak of the C–S was detected at 285.7 eV. The N 1 s spectrum (Figure S5b) exhibited binding energy peaks at 400.6 and 399.1 eV for C–N and C=N, respectively. The O 1 s spectrum (Figure S5c) displayed four peaks at 530.9, 532.3, 533.6, and 536.1 eV, which were attributed to C–O, –CHO, C=O and surface-adsorbed O_2 , respectively.^[34,35] The S 2p spectrum of TpBa and TpDa (Figure S5d) could be deconvoluted into two peaks with binding energies at 165.7 and 164.5 eV, represented the two 2p orbitals of S in C–S–C, proving the presence of benzothiazole.^[36] The ^{13}C solid-state nuclear magnetic

resonance (SSNMR) spectra of the three COFs (Figure S6) revealed carbon signals corresponding to distinct structural environments within the frameworks. These findings demonstrated that the three COFs were formed via Schiff base condensation reactions.

To better understand the significant differences of the three COFs, it is necessary to deeply explore their photocatalytic properties. The light absorption performance of the three COFs was measured and studied using UV–vis diffuse reflectance spectra (DRS). From Figure 2d, it could be observed that the signal intensities of TpBa and TpDa were higher than those of TpPa, indicating superior light absorption performance. Meanwhile, the bandgaps of TpBa, TpPa, and TpDa calculated using the Kubelka–Munk equation were 1.92, 2.12, and 1.95 eV, respectively. It was essential to consider the light absorption performance in liquid-phase system. The optical parameters of the three COFs were presented in Table S4, indicating that the suspension of TpBa exhibited higher light absorption performance. Meanwhile, analysis from Figure S7 and Table S5 revealed that the local volumetric rate of photon absorption (LVRPA), total rate of photon absorption (TRPA), and optical thickness of TpBa were higher than those of TpPa. TpDa approached TpBa in these metrics.^[37]

To investigate the charge transfer behavior, the fluorescence decay spectra and photoluminescence (PL) spectra of different materials were analyzed. As shown in Figure 2e, the fluorescence lifetime of TpBa (2.85 ns) was longer than those of TpPa (2.01 ns) and TpDa (2.36 ns), indicating that the photo-generated charge carriers in TpBa were less likely to recombine and possessed a higher separation efficiency. In the inset, the fluorescence intensity of TpBa was lower than those of TpPa and TpDa, demonstrating reduced recombination of photogenerated carriers. Femtosecond transient absorption spectroscopy (fs-TAS) was employed to investigate photo-generated electron dynamics in the visible region. Distinct negative ground-state bleach (GSB) signals were observed for all three COFs within the 515–550 nm range (Figure S8d–f). Fitting the decay kinetics of this spectral region (Figure 2f) revealed a markedly longer decay time constant for TpBa (180 ps) compared to TpPa (82 ps) and TpDa (142 ps). This prolonged relaxation time indicated extended lifetimes of photogenerated electrons and corresponded to slower electron-hole recombination kinetics.^[38] Therefore, by using C_{1h} symmetric benzothiazole ligand to synthesize TpBa, the separation efficiency of electron-hole pairs was improved, which would lead to enhanced photocatalytic performance.^[39]

The Mott–Schottky (M–S) curve (Figure S9) was used to evaluate the flat band potential (E_{fb}) of the catalyst. In the M–S curves diagram, the slopes of the three COFs indicated that they were n-type semiconductors. The flat band potentials of TpBa, TpPa and TpDa were -0.58 , -0.44 , and -0.55 eV (versus Ag/AgCl). Combined with M–S curve and optical band gap,^[40] the conduction band (CB) of the three COFs were calculated to be -0.48 , -0.34 , and -0.45 eV (versus NHE), and the valence band (VB) were calculated to be 1.54, 1.88 and 1.50 eV (versus NHE) (Figure 2g). The transient photocurrent-response intensity of TpBa, TpPa, and TpDa was determined in multiple intermittent visible light

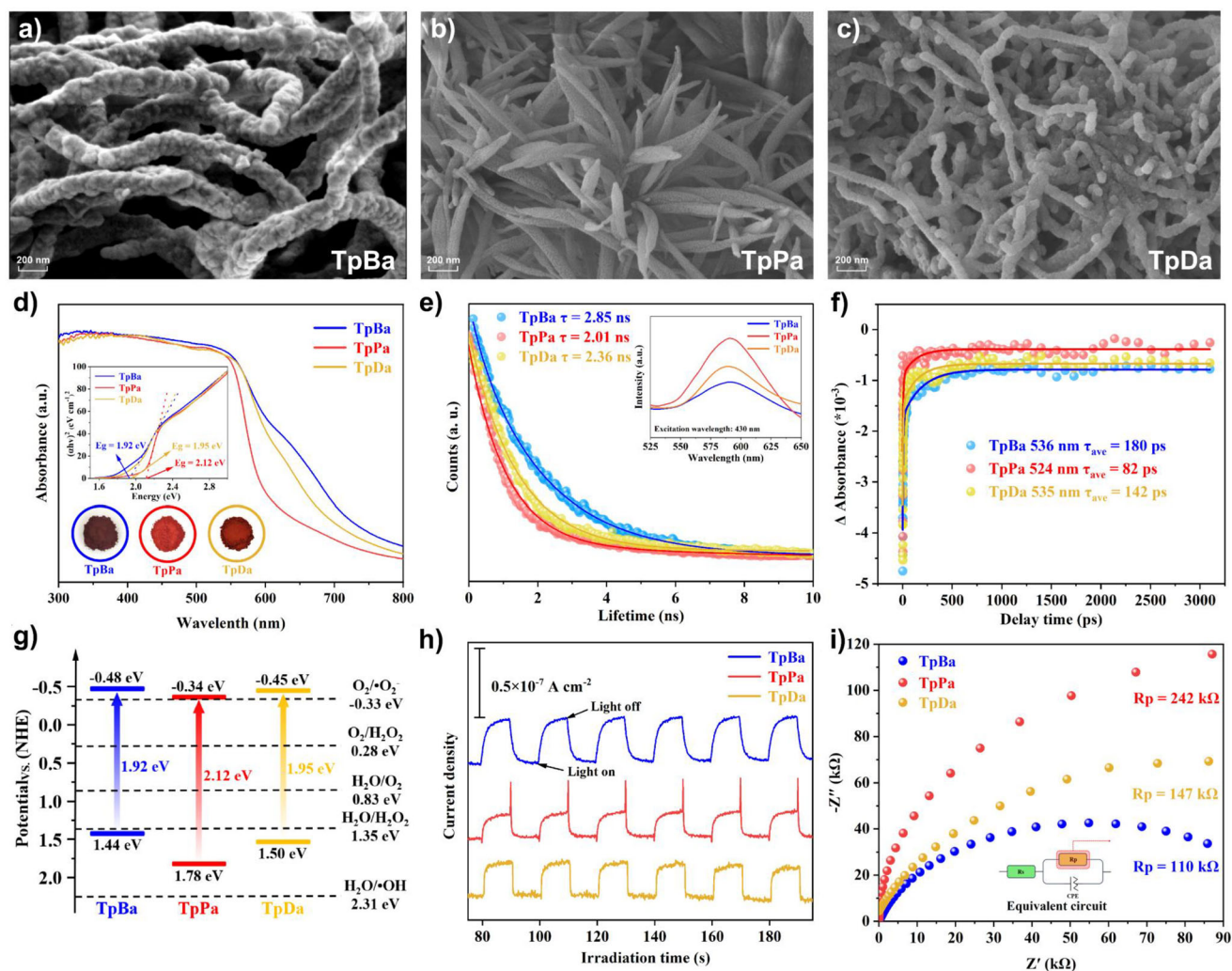


Figure 2. SEM images of TpBa a), TpPa b), and TpDa c). d) UV-vis absorption spectra, Tauc plots (insert), e) fluorescence decay spectra, PL spectra (insert), f) fs-TAS kinetic trace plots, g) experimental band alignment, h) photocurrent response and i) EIS Nyquist plot for TpBa, TpPa, and TpDa.

conditions. Figure 2h showed that TpBa exhibited higher photocurrent intensity. In contrast, TpPa showed a rapid increase in signal value immediately after the light source was turned off, generating a peak due to fast recombination of electrons and holes,^[41] which was not observed for TpBa and TpDa. Additionally, the interfacial charges transfer behavior of photocatalysts was further expounded by EIS. In the Nyquist plot (Figure 2i), the arc radius for TpBa was smaller than that for TpPa and TpDa, indicating lower charge transport resistance and accelerated interface electron transport rate.^[42] The unique structure of TpBa promotes the generation of photogenerated charge carriers, while its perfect planar conjugated system and heterocyclic framework further enhance the separation and transfer efficiency of photogenerated charge carriers.

We conducted a series of computational investigations on the periodic structures and molecular clusters of three COFs using the Multiwfn, CP2K, and other software packages.^[43,44] Under the optimized electronic structure, the band structures of TpBa, TpPa, and TpDa were investigated using DFT calculations. Additionally, in order to study the role of individual

atoms in constructing and controlling band structures and bandgaps, the density of states (DOS) for C, N, O, S, and H atomic orbitals as well as the total DOS (TDOS) were calculated for three COFs (Figures S10–S12). In the band structure diagrams, the first Brillouin zone was divided into Γ -K-M- Γ along a highly symmetric k direction. The band structures and DOS of TpBa, TpPa and TpDa were shown in Figure S13. The DOS analysis revealed that the O atoms contribute significantly to the formation of the CB. The minimum value of CB (CBM) and maximum value of VB (VBM) for all three COFs were depicted in Figure S14. The CBM is primarily localized on the ketonic six-membered ring, which is likely the region of electron density accumulation upon photoexcitation.

To further elucidate the transport dynamics of charges within the COFs framework, the electron localization function (ELF) was used to determine and describe the electron transport pathways. As shown in Figure S15, TpDa had more red highlighted areas than TpBa and TpPa due to the presence of benzobisthiazole. Thus TpDa had more electron transport pathways. The distribution of charge density (CD)

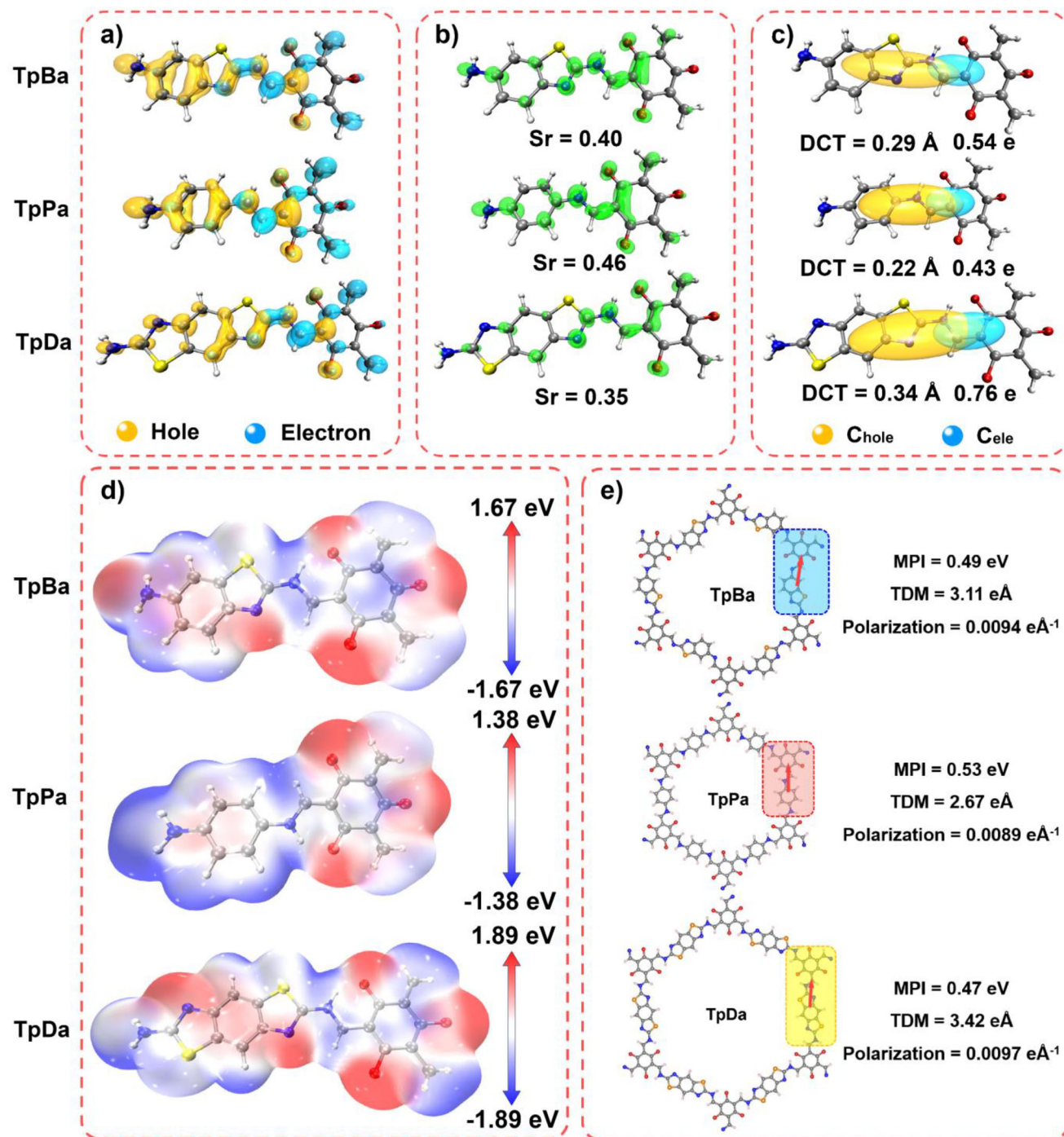


Figure 3. a) Electron-hole distribution diagrams, b) Sr overlap integral, c) $C_{\text{hole}}-C_{\text{ele}}$, d) ESP diagrams for TpBa, TpPa, and TpDa. e) The dipole moment schematic diagrams of TpBa, TpPa, and TpDa, as well as MPI, TDM, and polarizability.

reveals the actual spatial distribution of electrons within the structure. As observed in Figure S16, there was an increased quantity of negatively charged electrons in TpDa compared to TpBa and TpPa, which was also attributed to the presence of benzobisthiazole. A higher concentration of points with high charge density made charge transfer more likely.^[45]

Furthermore, the distribution of electrons and holes in the COFs fragments was simulated, as shown in Figure 3a. The holes in three COFs were basically concentrated in one seg-

ment of the amine linker, which served as an electron donor. The electrons were concentrated on the aldehyde ligand node, which served as an electron acceptor. Therefore, the studied fragments exhibited a simple D–A unit. We employed the Sr index, which was defined as the geometric mean of the electron-hole overlap. As shown in Figure 3b, the electron-hole overlap part in TpDa was smaller than that in TpBa and TpPa, with Sr (TpBa) = 0.40, Sr (TpPa) = 0.46 and Sr (TpDa) = 0.35. The smaller the integral index, the smaller the

electron-hole overlap rate, and the easier it is for the electron-hole pair to separate. The Sm index (Figure S17) was used to describe the minimum of the electron-hole overlap, and TpDa exhibited the minimal value for this index ($Sm(TpBa) = 0.18$, $Sm(TpPa) = 0.23$, and $Sm(TpDa) = 0.15$).^[46] The charge density difference (CDD) between the ground state and the excited state, and the charge centroid shift, were used to show the charge transfer. Quantitative analysis of charge transfer was based on Hirshfeld atomic charges corrected for atomic dipoles. The CDD was illustrated in Figure S18, while the charge center was depicted in Figure 3c. The charge center provided a more intuitive representation of the difference in charge density. The positive and negative charge centers ($C_{hole} - C_{ele}$) of the three COFs are located on the amine linker and aldehyde linker, respectively, corresponding to the electron-hole distribution. Distance of charge transfer (DCT) represents the distance between the centroid of the charge density increment region and the decrement region under electronic excitation. It measures how far charges jump upon excitation. Specifically, TpDa had a DCT value of 0.34 Å with electron transfer amount of 0.76 e. For TpBa and TpPa, these values were 0.29 and 0.22 Å, 0.54 and 0.43 e, respectively.^[47] Thus, TpDa exhibited stronger D–A unit action leading to enhanced efficiency in both charge separation and transport.

To better study the influence of the structure of COFs on the separation and transport of charges, we conducted an analysis of the electrostatic potential (ESP) distribution for three COFs. As shown in Figure 3d, the ESP distribution difference was not significant on the aldehyde ligand side, with O atoms exhibiting strong electronegativity and notable electron affinity. On the amine ligand side of TpBa and TpDa, thiazole structure has been observed to increase the distribution of high-energy equipotential surfaces, potentially enhancing local polarization and facilitating electron mobility.^[20] However, when studying the molecular polarity index (MPI) based on molecular structure and dipole moment, the MPI values for TpBa and TpDa were found to be 0.49 and 0.47 eV, which were smaller than that of TpPa (0.53 eV). This occurs because the calculated fragment areas of TpBa and TpDa were larger than that of TpPa, resulting in partial steric hindrance that restricts the optimal charge separation orientation within the D–A units. MPI primarily studies the dipole moment and polar properties of COFs in their ground state. Interestingly, when simulating the dipole moment direction (Figure 3e), the resulting transition dipole moment (TDM) of TpDa (3.42 eÅ) was greater than those of TpBa (3.11 eÅ) and TpPa (2.67 eÅ). This was related to the superiority of TpDa's charge distribution and structure. In other words, after being excited by light, there was a higher probability of electron transition, and the improved electron cloud arrangement was more conducive to charge separation and transport. The calculated fragment area was used to calculate the polarizability (polarizability = TDM/unit fragment area, $S(TpBa) = 330 \text{ \AA}^2$, $S(TpPa) = 300 \text{ \AA}^2$, and $S(TpDa) = 358 \text{ \AA}^2$). Calculations yielded a polarizability of 0.0097 e\AA^{-1} for TpDa, while values of 0.0094 and 0.0089 e\AA^{-1} were obtained for TpBa and TpPa, respectively.^[48]

While TpDa exhibited favorable charge distribution and structural features, these computational advantages were

not consistent with the experimental results obtained from photoelectrochemical measurements and spectroscopic characterizations. Thus, we further explored other factors from the molecular structure of COFs. The AIRT effect first considers the angle between the two ends of the linker. The angle between the amine ligand-connected ends of the TpBa linker was 158.7° , the corresponding angles for the TpPa and TpDa linkers were both 180.0° . TpPa and TpDa were basically linearly connected. One key factor affecting the twist of COFs is the interlayer force, which belongs to non-covalent intermolecular (NCI) forces. The 2D mapping diagrams of NCI were shown in Figure 4a–c. In order to fully consider the NCI of the C_{1h} symmetrical linkers, we constructed a $1 \times 1 \times 3$ unit cell for three COFs as the calculation model, and twisted the aromatic rings on the linker in the second layer along the β -ketoenamine bond by different angles, fixing the rest, and calculated the NCI between layers. The NCI of the three COFs was not significant at rotation angles of 0° and -20° . At 40° , the benzothiazole linker of TpBa showed a stronger red repulsive region, making twisting more difficult. At angle of 60° , the repulsive region increased, and the atoms in this layer were close to the bonding orbitals of the atoms in the upper layer, making it difficult to twist to this position. The linkers of TpPa and TpDa also received some repulsive force influence during the twisting process, but the rendering area of the repulsive force was smaller than that of TpBa. Consequently, TpPa and TpDa undergo molecular planar twisting more readily.^[49] The characteristics of π -electron delocalization in COFs under linker twisting were investigated using the localized orbital locator of π -electrons (LOL- π). As depicted in Figure 4d, at a torsional angle of 40° , discernible disruptions in the electron delocalization pathways were observed at the bonding sites for both TpPa and TpDa, relative to the planar conformation (0°). This clearly demonstrated that torsional distortion disrupted the planar π -conjugated system.^[50]

When constructing structures with different torsional angles, TpPa and TpDa can twist normally, but the molecular structure of TpBa undergoes distortion due to the AIRT effect during the twisting process. Based on the NCI, to further elucidate the mechanisms of the enhancement of electronic motion and photocatalysis by the AIRT effect, we also calculated the binding energy, total electronic energy, and rotational potential barrier. As shown in Figure 5a, in the initial state (0°), the C_{1h} symmetrical linker of TpBa was attracted, with binding energy of -3.11 eV , while the binding energy of TpPa (0.40 eV) and TpDa (2.56 eV) was weaker. Upon twisting the linker by 60° , binding energy of TpBa rapidly increased to 7.67 eV. Meanwhile, significant repulsion was exerted on the C_{1h} symmetric benzothiazole linkers, causing quick return to its initial planar state. Conversely, only weak repulsion affects the benzene ring on linker of TpPa, resulting in binding energy of 0.40 eV, while that of the benzobisthiazole in TpDa was only 2.56 eV. At angles in the range of $\pm 40 - \pm 60^\circ$, the repulsive force increased as the two atomic layers approach each other. However, under the AIRT effect, due to the special angle of the C_{1h} linkers, the atoms between the layers of TpBa became closer, resulting in a more significant increase in repulsive force compared to TpPa. Although the S atoms in TpDa also contributed to

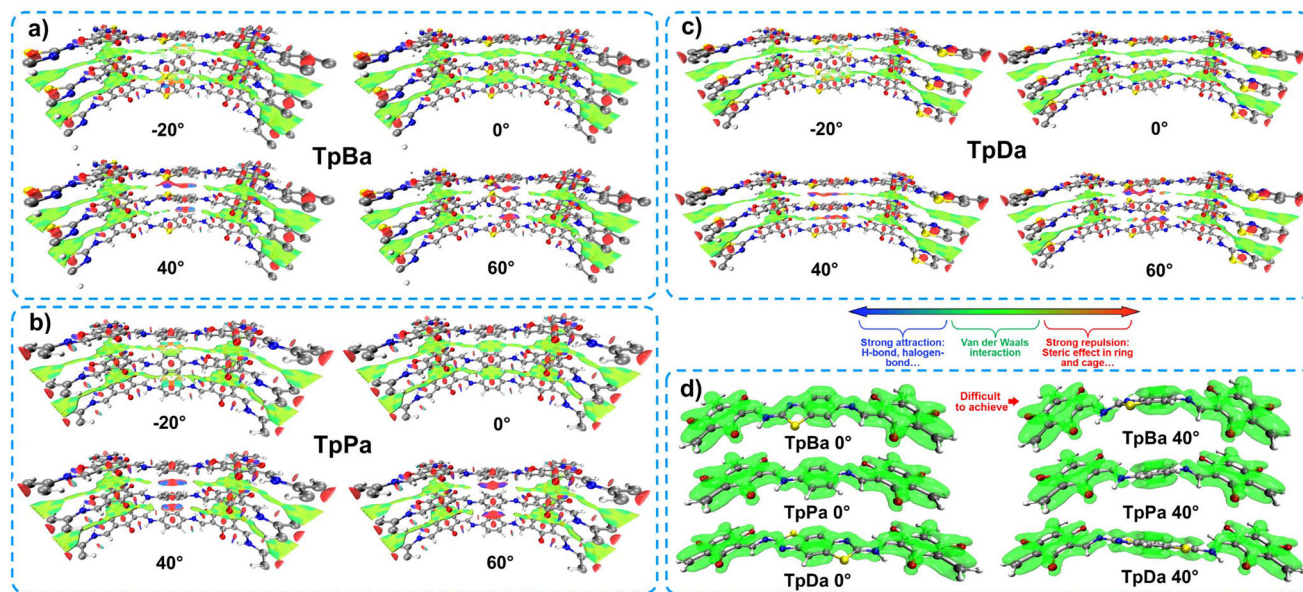


Figure 4. The non-covalent intermolecular (NCI) 2D mapping diagrams of TpBa a), TpPa b), and TpDa c). d) LOL- π isosurfaces of TpBa, TpPa, and TpDa.

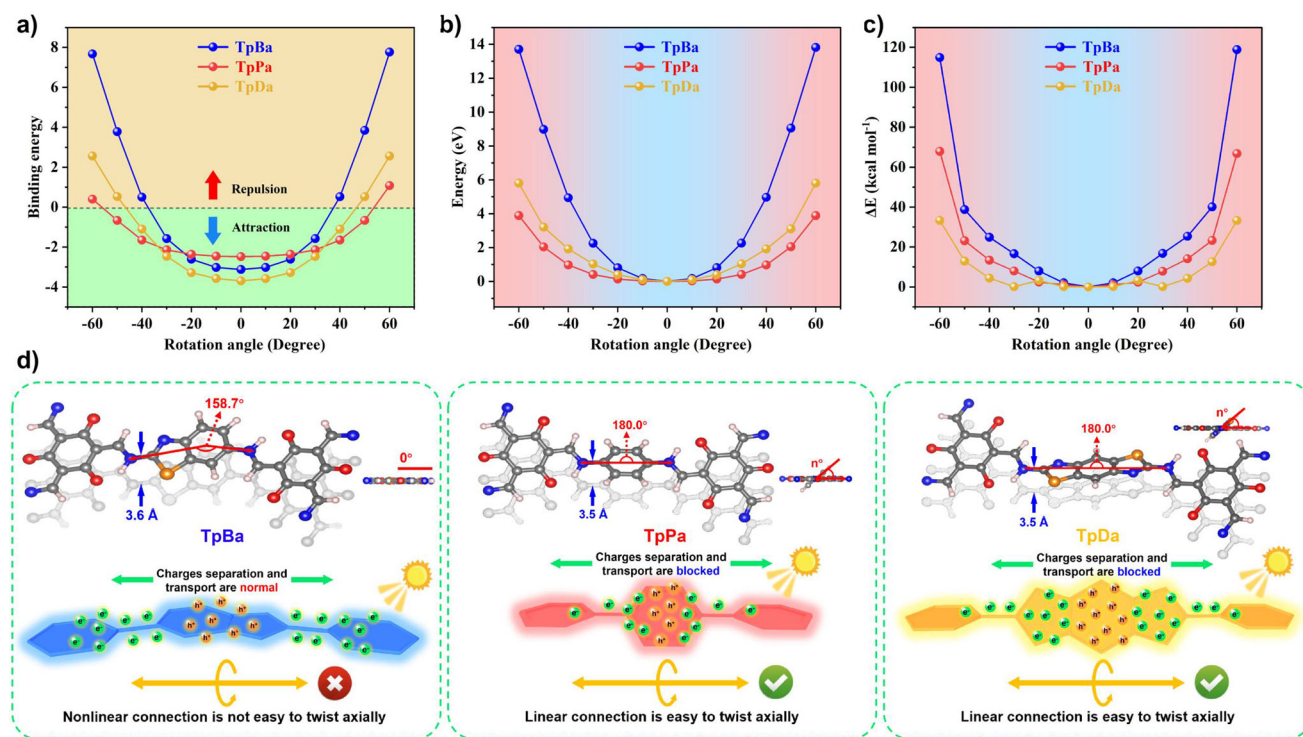


Figure 5. The binding energy a) of TpBa, TpPa, and TpDa at different torsional angles of the linker, the total electronic energy of the system b), and the rotational potential barrier (c). d) Under the AIRT effect, the impact of different twisting conditions of TpBa, TpPa, and TpDa on charge.

repulsion, it remained less pronounced than that observed in TpBa. In Figure 5b, as the twist angle increased, the total electronic energy of TpBa rose rapidly, especially at 60°, the total electronic energy was 13.81 eV, which was 3.57 times that of TpPa (3.88 eV) and 2.36 times that of TpDa (5.80 eV). TpBa needs more energy to achieve linker twist,

and the structure becomes unstable under twist, which will make it quickly return to the plane stable state. Concurrently, Figure 5c demonstrated that TpBa exhibited a higher rotating potential barrier than both TpPa and TpDa, indicating greater resistance to twisting in TpBa. Since the energy change of single-layer structure is considered in the rotating potential

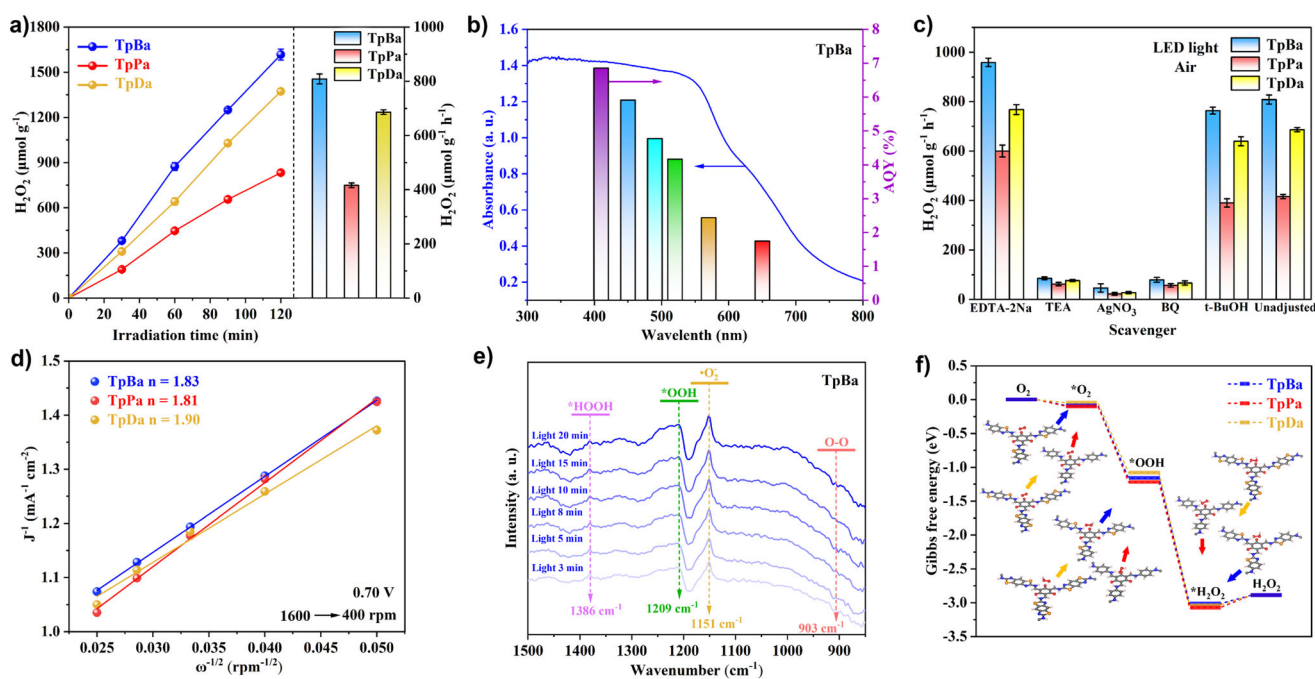


Figure 6. a) The performances of TpBa, TpPa and TpDa for H₂O₂ photoproduction ($C_{\text{cat.}} = 50 \text{ mg L}^{-1}$, 295 K, LED light, Air). b) AQY of TpBa at selected wavelengths (410, 450, 490, 520, and 650 nm). c) The H₂O₂ yields of TpBa, TpPa, and TpDa with different scavengers. d) The Koutechy-Levich plots of TpBa, TpPa and TpDa (400–1600 rpm). e) In situ DRIFTS of TpBa collected in the H₂O₂ photocatalytic processes in the O₂ atmosphere. f) Gibbs free energy diagram of the TpBa, TpPa and TpDa for photocatalytic H₂O₂ synthesis by the indirect 2e⁻ ORR path.

barrier, the main factor leading to the energy change gap is the angle of nonlinear connection rather than NCI. The larger the angle, the more obvious the AIRT effect. Especially at 60°, the energy barrier difference between TpBa and the other two COFs was the largest, and TpBa was more difficult to twist.^[51] In conjugated macromolecular systems, stabilization is delocalized across numerous atoms and bonds, resulting in smaller energy changes during twisting. Consequently, TpDa exhibited the lowest rotational potential barrier among the three COFs. Figure 5d was the schematic diagram of AIRT effect. In the circular dichroism (CD) spectrum of the three achiral COFs (Figure S19), TpBa exhibited a negligible CD signal, whereas TpPa and TpDa showed weak signals, likely induced by molecular plane twisting. This suggested that TpBa possessed a more rigid planarity.^[52] In addition, in situ variable-temperature XRD (VT-XRD) measurement was conducted to investigate the twist behavior at the crystalline level. According to Bragg law (Equation 1), with a fixed X-ray wavelength λ , the diffraction angle θ (2–30°) is inversely proportional to the interplanar spacing d . Therefore, for 2D π - π stacked materials, a shift of the (0 0 1) diffraction peak toward lower angles indicates an expansion of the interlayer spacing. As shown in Figure S20, when the temperature was increased from 25 to 120 °C, the (0 0 1) diffraction peak of TpBa shifted by 0.34°, which can be attributed to conventional thermal expansion. In contrast, larger shifts of 0.66° and 0.71° were observed for TpPa and TpDa, respectively. We speculated that the molecular layers in TpPa and TpDa were more prone to torsional deformation, and that such twisted molecular planes facilitated greater expansion of the interlayer spacing during heating.^[53]

$$n * \lambda = 2 * d * \sin \theta \quad (1)$$

The photocatalytic performance of catalysts was evaluated through the generation of H₂O₂ under visible light irradiation. The reaction was conducted in pure water without any sacrificial agents under air atmosphere and LED light. As shown in Figure 6a, TpBa displayed a notable photoactivity of 808.8 μmol g⁻¹ h⁻¹. TpDa demonstrated a slightly lower rate of 686.4 μmol g⁻¹ h⁻¹, whereas the H₂O₂ generation rate detected for TpPa was significantly reduced at 416.1 μmol g⁻¹ h⁻¹. As shown in Figure S21a, under the irradiation of a Xe lamp ($\lambda \geq 400 \text{ nm}$), the yields of TpBa, TpPa and TpDa increased to 987.5, 494.2 and 830.8 μmol g⁻¹ h⁻¹, respectively. In Figure S21b, under the condition of fully aerated reactor with O₂, the H₂O₂ yield of TpBa was increased to 1163.5 μmol g⁻¹ h⁻¹, which was 43.8% increase compared to that under air. In contrast, under N₂ atmosphere, TpBa exhibited a poor H₂O₂ yield (97.0 μmol g⁻¹ h⁻¹), which was only 12.0% of that under air atmosphere. TpPa and TpDa also showed the similar phenomenon. It can be inferred that the three COFs likely produce H₂O₂ through the oxygen reduction reaction (ORR).^[54] Furthermore, through the decomposition experiment of H₂O₂ (Figure S21c), it can be observed that all three COFs have low activation ability for the decomposition of H₂O₂, and the decomposition rate was improved under LED and Xe lamp irradiation. Apparent quantum yield (AQY) (Figures 6b and S21d,e) was measured under monochromatic light irradiation at various wavelengths. At 420 nm, TpBa exhibited an AQY of 6.86%, surpassing those of TpPa (3.54%) and TpDa (5.75%). Additionally, TpBa achieved a solar-to-chemical conversion

(SCC) efficiency of 0.26%, also higher than TpPa (0.13%) and TpDa (0.22%).^[51]

Different scavengers were introduced into the reactor to speculate possible intermediate products involved in the reaction. The results were depicted in Figure 6c. It was evident that upon the addition of AgNO₃ and benzoquinone (BQ) to capture e⁻ and •O₂⁻, the H₂O₂ yield of TpBa decreased to 46.3 and 79.1 μmol g⁻¹ h⁻¹, respectively. Although both the indirect 2e⁻ ORR and the direct 2e⁻ ORR are thermodynamically possible, the experimental results confirmed that •O₂⁻ was an important intermediate product, and the 2e⁻ ORR was the primary pathway. Upon the addition of tert-butanol (TBA) to capture •OH, a slight decrease in yield was observed, indicating the presence of a small fraction of 2e⁻ water oxidation reaction (WOR).^[55] Furthermore, upon capturing holes with EDTA-2Na, the H₂O₂ yields of all three COFs increased moderately. In contrast, the use of triethanolamine (TEA) resulted in a significant decrease in yield. This behavior is attributed to the fact that holes oxidize H₂O, generating H⁺ which participates in the formation reaction. TEA blocks this water oxidation pathway. Conversely, although EDTA-2Na reacts with holes, it still facilitates the generation of H⁺ and thus does not impede H₂O₂ production. To briefly validate this hypothesis, comparative experiments were conducted in H₂O and D₂O. As shown in Figure S21f, upon addition of EDTA-2Na, the yield of H₂O₂ increased, whereas that of D₂O₂ was lower compared to the untreated reaction mixture. This indicated that EDTA-2Na may act as a proton source during the photocatalytic process.^[56] Furthermore, monitoring the reaction pH (Figure S21g) revealed that the introduction of EDTA-2Na led to a decrease in pH. As the reaction proceeded, a further slight decline in pH was observed, indicating the continuous release of protons.^[57] To precisely determine the oxygen source during the reaction, complementary isotope labeling experiments were undertaken. As shown in Figure S21h, the reaction of ¹⁸O₂ with H₂¹⁶O yielded H₂¹⁸O₂ at a molar concentration comparable to that of H₂¹⁶O₂ in the control group. In contrast, the reaction of ¹⁶O₂ with H₂¹⁸O produced a significantly lower concentration of H₂¹⁸O₂ relative to H₂¹⁶O₂.^[58] These results demonstrated that O₂ served as the primary oxygen source for H₂O₂ generation.

Additionally, the linear sweep voltammetry (LSV) curves of the three COFs at different rotational speeds (from 400 to 1600 rpm) were measured using a rotating ring-disk electrode (RRDE), as shown in Figure S22. By plotting the curves using the Koutecky–Levich method, the electron transfer numbers for TpBa, TpPa, and TpDa were respectively calculated to be 1.83, 1.81, and 1.90 (0.70 V) (Figure 6d). Besides, the electron transfer number was also nearly two, with TpBa outperforming TpPa and TpDa in H₂O₂ selectivity (Figure S23a). The Tafel slope (Figure S23b) was plotted from the LSV curve at 1225 rpm, revealed that TpBa exhibited a smaller slope, indicating more favorable ORR activity.^[31]

Electron paramagnetic resonance (EPR) analysis was utilized to detect the presence of intermediate radicals. As evidenced by the EPR spectra in Figure S24a,b, signals corresponding to •OH and •O₂⁻ exhibited notably greater

intensity for TpBa than for TpPa and TpDa after 5 min of reaction. To qualitatively assess •O₂⁻ and •OH, the nitro blue tetrazolium (NBT) method (Figure S25) and terephthalic acid (TA) method (Figure S26) were also explored.^[59] Our findings demonstrated that the yield of •O₂⁻ was approximately an order of magnitude higher than that of •OH. Another characteristic 2e⁻ ORR product, •OOH, was also detected, with TpBa once again exhibiting the most intense signal (Figure S24c). In addition, this process over TpBa was revealed by in situ diffuse reflectance infrared Fourier transform spectroscopy (DRIFTS) studies. As exhibited in Figure 6e, the increasing peaks at 1209 and 1151 cm⁻¹ correspond to the vibration of *OOH and •O₂⁻. These intermediates verified the 2e⁻ ORR path again.^[60] In order to gain a more profound understanding of the active sites and reaction mechanisms of the three COFs, DFT calculations were also performed. We created O₂ adsorption models and selected sites based on their adsorption energies for subsequent Gibbs free energy calculations. In Table S6, the adsorption energy of the ketonic six-membered ring junctions in the three COFs was the highest, making them the primary adsorption sites for O₂ molecules. These sites were electron-rich, which aligned with the computational results mentioned earlier. As evidenced by the thermodynamic analysis in Figure 6f, the Gibbs free energy for each reaction step of TpBa was comparable to those of TpPa and TpDa, attributed to their common adsorption-reaction sites.^[61] Meanwhile, the competing 4e⁻ ORR pathway was also evaluated. As shown in Figure S27, the conversion of *OOH to *O on the three COFs is associated with a positive Gibbs free energy change, indicating that the 4e⁻ pathway is energetically unfavorable and requires stringent conditions. Consequently, the reaction favors the production of *H₂O₂, demonstrating high selectivity for the 2e⁻ pathway.^[62,63] Based on the kinetic isotope effect (KIE) data (KIE = 1.63) presented in Figure S21f (left) and the results in Figure S28, it can be concluded that the supply of protons influences the yield of H₂O₂ to some extent. Therefore, the proton-coupled electron transfer (PCET) process plays a significant role in the reaction.^[64] The enhanced photocatalytic performance of TpBa is attributed to the AIRT effect, which sustains efficient charge separation and transport, thereby enabling greater electron participation in the formation of •O₂⁻, *OOH, and *H₂O₂.

TpBa maintains a comparable level of H₂O₂ yield to several reported COFs that require Xe lamp irradiation or oxygen aeration conditions (Table S7). On the other hand, the benzothiazole unit in TpBa exhibits superior performance with respect to both the Sr index and TDM compared to its two analogous fused heterocycles, benzoxazole and benzimidazole (Figure S29). Compared to commercial photocatalysts like g-C₃N₄, TpBa demonstrated superior performance in H₂O₂ production (Figure S30). To assess the stability of TpBa, we monitored its H₂O₂ yield over multiple cycles. The results presented in Figure S31a demonstrated that TpBa exhibited excellent stability for H₂O₂ generation across 10 consecutive cycles. The PXRD pattern of the sample after cycling (Figure S31b) showed no significant difference compared to the initial sample, indicating its excellent

photostability. Furthermore, the PXRD patterns of TpBa remained virtually unchanged after soaking in strongly acidic (pH = 1) and strongly alkaline (pH = 13) solutions for 3 days, confirming its exceptional chemical stability. To explore the potential for practical application of TpBa, we conducted a long-duration H₂O₂ production experiment. As shown in Figure S31c, TpBa maintained stable H₂O₂ output during a 24 h continuous photocatalytic reaction. Additionally, a scaled-up experiment under ambient sunlight conditions was performed. Figure S31d revealed that TpBa also achieved a favorable H₂O₂ yield under natural sunlight irradiation. (details regarding the scaled-up reactor specifications and experimental conditions can be found in Text S13 and Figure S31e).

Conclusion

In summary, this work reported a novel COF TpBa with β -ketoenamine bonds using C_{1h} symmetric benzothiazole as linker. Compared to TpPa with a phenyl linker, TpBa demonstrated boosted photocatalytic performances (e.g., TpBa exhibited H₂O₂ yield of 808.8 $\mu\text{mol g}^{-1} \text{h}^{-1}$, which was ca. 2 times that of TpPa). Furthermore, TpBa unexpectedly outperformed TpDa in both various characterization metrics and photocatalytic performances, despite TpDa possessing a theoretically more favorable charge structure and distribution. To explain this phenomenon, an AIRT effect resulting from non-linear connections at both ends of the C_{1h} symmetric ligand was proposed for the first time, which increased the NCI when twisted and led to system energy instability before returning to its flat state. This limitation on molecular plane twist maintained planar π -conjugated systems within COFs skeletons, ensuring normal charge separation and transport, and ultimately boosting photocatalytic performance. Our work represented an exploration into a new approach for synthesizing COFs using C_{1h} symmetric linkers. Strategies about twist and planar π -conjugated system structure-activity relationship will be beneficial for regulating COFs with target applications.

Acknowledgements

This work was supported by the National Natural Science Foundation of China (No. 22276168), “Pioneer” and “Leading Goose” R&D Program of Zhejiang (2025C02240). Partial support from the Robert A. Welch Foundation (B-0027) (S.M.) and the Ongoing Research Funding Program (ORF-2025–79), King Saud University, Riyadh, Saudi Arabia (A.N.) is also acknowledged. The authors would like to thank the High-Performance Computing Platform of YuanSuan (yuansuan.top), and the shiyanjia lab (www.shiyanjia.com) for the VT-XRD test.

Conflict of Interests

The authors declare no conflict of interest.

Data Availability Statement

The data that support the findings of this study are available from the corresponding author upon reasonable request.

Keywords: Asymmetric ligands • Covalent organic frameworks • H₂O₂ • Photocatalysis • Planar twist

- [1] X. Feng, X. Ding, D. Jiang, *Chem. Soc. Rev.* **2012**, *41*, 6010–6022.
- [2] M. S. Lohse, T. Bein, *Adv. Funct. Mater.* **2018**, *28*, 1705553.
- [3] J. Wang, S. Zhuang, *Coordin. Chem. Rev.* **2019**, *400*, 213046.
- [4] H. Cheng, T. Wang, *Adv. Synth. Catal.* **2021**, *363*, 144–193.
- [5] X. Liu, D. Huang, C. Lai, G. Zeng, L. Qin, H. Wang, H. Yi, B. Li, S. Liu, M. Zhang, *Chem. Soc. Rev.* **2019**, *48*, 5266–5302.
- [6] Q. Yang, M. Luo, K. Liu, H. Cao, H. Yan, *Appl. Catal. B Environ. Energy* **2020**, *276*, 119174.
- [7] P. J. Waller, F. Gándara, O. M. Yaghi, *Accounts Chem. Res.* **2015**, *48*, 3053–3063.
- [8] K. Xiong, Y. Wang, F. Zhang, X. Li, X. Lang, *Appl. Catal. B Environ. Energy* **2023**, *322*, 122135.
- [9] M. Zhang, X. Song, M. Yao, C. Hao, J. Qiu, *J. Phys. Chem. Lett.* **2019**, *10*, 7445–7451.
- [10] H. Wang, H. Wang, Z. Wang, L. Tang, G. Zeng, P. Xu, M. Chen, T. Xiong, C. Zhou, X. Li, *Chem. Soc. Rev.* **2020**, *49*, 4135–4165.
- [11] C. S. Diercks, O. M. Yaghi, *Science* **2017**, *355*, eaall585.
- [12] W. Chen, P. Chen, D. Chen, Y. Liu, G. Zhang, L. Wang, L. Chen, *Adv. Sci.* **2022**, *9*, 2105517.
- [13] J. W. Colson, W. R. Dichtel, *Nat. Chem.* **2013**, *5*, 453–465.
- [14] R. Liu, K. Tan, Y. Gong, Y. Chen, Z. Li, S. Xie, T. He, Z. Lu, H. Yang, D. Jiang, *Chem. Soc. Rev.* **2021**, *50*, 120–242.
- [15] L. Jin, M. Deng, J. Gao, L. Wang, Q. Zhou, X. Tang, Q. Li, H. Du, D. Hao, Q. Wang, *Chem. Eng. J.* **2025**, *515*, 163722.
- [16] L. Wang, H. Du, X. Wang, D. Hao, Q. Li, H. Zhu, C. Li, Q. Wang, *Environ. Res.* **2025**, *272*, 121116.
- [17] C. Qian, L. Feng, W. L. Teo, J. Liu, W. Zhou, D. Wang, Y. Zhao, *Nat. Rev. Chem.* **2022**, *6*, 881–898.
- [18] L. Cusin, H. Peng, A. Ciesielski, P. Samorì, *Angew. Chem. Int. Ed.* **2021**, *133*, 14356–14370.
- [19] S. Wan, F. Gándara, A. Asano, H. Furukawa, A. Saeki, S. K. Dey, L. Liao, M. W. Ambrogio, Y. Y. Botros, X. Duan, *Chem. Mater.* **2011**, *23*, 4094–4097.
- [20] H. Yang, M. Hao, Y. Xie, X. Liu, Y. Liu, Z. Chen, X. Wang, G. I. Waterhouse, S. Ma, *Angew. Chem. Int. Ed.* **2023**, *135*, e202303129.
- [21] M. Wang, Z. Wang, M. Shan, J. Wang, Z. Qiu, J. Song, Z. Li, *Chem. Mater.* **2023**, *35*, 5368–5377.
- [22] H. Zhao, Y. Wang, F. Zhang, X. Dong, X. Lang, *Appl. Catal. B Environ. Energy* **2024**, *350*, 123899.
- [23] M. C. Daugherty, E. Vitaku, R. L. Li, A. M. Evans, A. D. Chavez, W. R. Dichtel, *Chem. Commun.* **2019**, *55*, 2680–2683.
- [24] L. Zhang, Q. Zhu, Y. Zhou, S. Wang, J. Fu, J. Liu, G. Zhang, L. Ma, G. Tao, G. Tao, *Nat. Commun.* **2023**, *14*, 8181.
- [25] K. Sun, Y. Huang, F. Sun, Q. Wang, Y. Zhou, J. Wang, Q. Zhang, X. Zheng, F. Fan, Y. Luo, *Nat. Chem.* **2024**, *16*, 1638–1646.
- [26] J. L. Segura, S. Royuela, M. M. Ramos, *Chem. Soc. Rev.* **2019**, *48*, 3903–3945.
- [27] K. Xiong, Y. Wang, F. Huang, K. Zhang, B. Zeng, X. Lang, *J. Colloid Interf. Sci.* **2024**, *665*, 252–262.
- [28] J. Chakraborty, A. Chatterjee, K. Molken, I. Nath, D. Arenas Esteban, L. Bourda, G. Watson, C. Liu, D. Van Thourhout, S. Bals, *Adv. Mater.* **2024**, *36*, 2314056.
- [29] Y. H. Kim, N. Kim, J. M. Seo, J. P. Jeon, H. J. Noh, D. H. Kweon, J. Ryu, J. B. Baek, *Chem. Mater.* **2021**, *33*, 8705–8711.

- [30] L. Yin, Y. Zhao, Y. Xing, H. Tan, Z. Lang, W. Ho, Y. Wang, Y. Li, *Chem. Eng. J.* **2021**, *419*, 129984.
- [31] W. Huang, Y. Hu, Z. Qin, Y. Ji, X. Zhao, Y. Wu, Q. He, Y. Li, C. Zhang, J. Lu, *Nat. Sci. Rev.* **2023**, *10*, nwac171.
- [32] S. Kandambeth, A. Mallick, B. Lukose, M. V. Mane, T. Heine, R. Banerjee, *J. Am. Chem. Soc.* **2012**, *134*, 19524–19527.
- [33] S. Karak, S. Kandambeth, B. P. Biswal, H. S. Sasmal, S. Kumar, P. Pachfule, R. Banerjee, *J. Am. Chem. Soc.* **2017**, *139*, 1856–1862.
- [34] Q. Cao, L. Zhang, C. Zhou, J. He, A. Marcomini, J. Lu, *Appl. Catal. B Environ. Energy* **2021**, *294*, 120238.
- [35] C. Li, M. Gao, X. Sun, H. Tang, H. Dong, F. Zhang, *Appl. Catal. B Environ. Energy* **2020**, *266*, 118586.
- [36] Q. Li, Q. Zhou, H. Deng, Z. Li, B. Xue, A. Liu, B. Shen, D. Hao, H. Zhu, Q. Wang, *Appl. Catal. B Environ. Energy* **2025**, *360*, 124533.
- [37] J. Li, D. Wang, S. Zhao, R. Ma, J. Guo, Z. Li, D. Wang, Y. Xuan, L. Wang, *Appl. Catal. B Environ. Energy* **2024**, *351*, 124007.
- [38] T. Xu, Z. Wang, W. Zhang, S. An, L. Wei, S. Guo, Y. Huang, S. Jiang, M. Zhu, Y. Zhang, *J. Am. Chem. Soc.* **2024**, *146*, 20107–20115.
- [39] X. Li, Q. Gao, J. Wang, Y. Chen, Z. Chen, H. Xu, W. Tang, K. Leng, G. Ning, J. Wu, *Nat. Commun.* **2018**, *9*, 2335.
- [40] Z. Huang, X. Li, L. Mei, Y. Han, Y. Song, X. Fu, Z. Zhang, Z. Guo, J. Zeng, F. Bian, *Adv. Funct. Mater.* **2024**, *34*, 2404126.
- [41] A. Sarkar, K. Karmakar, G. G. Khan, *J. Phys. Chem. C* **2017**, *121*, 25705–25717.
- [42] B. Shen, H. Du, A. Liu, N. Li, C. Chen, L. Shen, Y. Hui, R. Huo, Z. Zhang, Q. Wang, *J. Clean. Prod.* **2025**, *523*, 146458.
- [43] T. Lu, F. Chen, *J. Comput. Chem.* **2012**, *33*, 580–592.
- [44] T. D. Kühne, M. Iannuzzi, M. Del Ben, V. V. Rybkin, P. Seewald, F. Stein, T. Laino, R. Z. Khaliullin, O. Schütt, F. Schiffmann, *J. Chem. Phys.* **2020**, *152*, 19.
- [45] Y. Shang, W. Li, Y. Ma, B. Li, Q. Xu, Y. Du, Y. Peng, Y. Wang, Y. Zhu, *Adv. Funct. Mater.* **2024**, *34*, 2406533.
- [46] Z. Chen, J. Wang, M. Hao, Y. Xie, X. Liu, H. Yang, G. I. Waterhouse, X. Wang, S. Ma, *Nat. Commun.* **2023**, *14*, 1106.
- [47] Y. Qian, Y. Han, X. Zhang, G. Yang, G. Zhang, H. Jiang, *Nat. Commun.* **2023**, *14*, 3083.
- [48] F. Liu, P. Zhou, Y. Hou, H. Tan, Y. Liang, J. Liang, Q. Zhang, S. Guo, M. Tong, J. Ni, *Nat. Commun.* **2023**, *14*, 4344.
- [49] H. Sajid, M. Asif, K. Ayub, M. A. Gilani, M. S. Akhter, T. Mahmood, *S. Interf.*, **2021**, *27*, 101587.
- [50] F. Yu, C. Li, W. Li, Z. Yu, Z. Xu, Y. Liu, B. Wang, B. Na, J. Qiu, *Adv. Funct. Mater.* **2024**, *34*, 2307230.
- [51] Y. Mou, X. Wu, C. Qin, J. Chen, Y. Zhao, L. Jiang, C. Zhang, X. Yuan, E. Huixiang Ang, H. Wang, *Angew. Chem. Int. Ed.* **2023**, *62*, e202309480.
- [52] N. Berova, L. Di Bari, G. Pescitelli, *Chem. Soc. Rev.* **2007**, *36*, 914–931.
- [53] G. M. Dontireddy, S. P. Suman, J. L. Merino Gardea, A. H. Javed, J. Wang, T. Chen, S. Kampouri, H. Banda, *J. Mater. Chem. A* **2025**, *13*, 8734–8741.
- [54] X. Zhang, S. Cheng, C. Chen, X. Wen, J. Miao, B. Zhou, M. Long, L. Zhang, *Nat. Commun.* **2024**, *15*, 2649.
- [55] Q. Liao, Q. Sun, H. Xu, Y. Wang, Y. Xu, Z. Li, J. Hu, D. Wang, H. Li, K. Xi, *Angew. Chem. Int. Ed.* **2023**, *62*, e202310556.
- [56] L. Li, Q. Bu, T. Lang, R. Zhang, Y. Pang, Y. Zhang, Y. Lin, D. Wang, T. Xie, D. Wang, *Angew. Chem. Int. Ed.* **2025**, *137*, e202501357.
- [57] X. Luo, S. Zhou, S. Zhou, X. Zhou, J. Huang, Y. Liu, D. Wang, G. Liu, P. Gu, *Adv. Funct. Mater.* **2025**, *35*, 2415244.
- [58] W. Chi, Y. Dong, B. Liu, C. Pan, J. Zhang, H. Zhao, Y. Zhu, Z. Liu, *Nat. Commun.* **2024**, *15*, 5316.
- [59] J. Yue, L. Song, Y. Fan, Z. Pan, P. Yang, Y. Ma, Q. Xu, B. Tang, *Angew. Chem. Int. Ed.* **2023**, *62*, e202309624.
- [60] T. Yang, D. Zhang, A. Kong, Y. Zou, L. Yuan, C. Liu, S. Luo, G. Wei, C. Yu, *Angew. Chem. Int. Ed.* **2024**, *136*, e202404077.
- [61] Y. Guo, Y. Dong, B. Liu, B. Ni, C. Pan, J. Zhang, H. Zhao, G. Wang, Y. Zhu, *Adv. Funct. Mater.* **2024**, *34*, 2402920.
- [62] J. Yang, H. Yin, A. Du, M. Tebyetekerwa, C. Bie, Z. Wang, Z. Sun, Z. Zhang, X. Zeng, X. Zhang, *Appl. Catal. B Environ. Energy* **2025**, *361*, 124586.
- [63] H. Du, B. Shen, R. Huo, Y. Hui, C. Chen, A. Liu, Z. Zhang, C. Li, B. Ni, D. Hao, Q. Wang, *Appl. Catal. B: Environ. Energy* **2025**, *379*, 125688.
- [64] C. Wang, H. Li, F. Shen, S. Ge, X. Zhang, J. Ma, K. Zhang, J. Qian, B. Pan, *Appl. Catal. B Environ. Energy* **2025**, *361*, 124672.

Manuscript received: August 17, 2025

Revised manuscript received: September 11, 2025

Manuscript accepted: September 12, 2025

Version of record online: September 22, 2025